

Self-enhanced mobility enables vortex pattern formation in living matter

<https://doi.org/10.1038/s41586-024-07114-8>

Haoran Xu¹ & Yilin Wu¹✉

Received: 1 February 2023

Accepted: 24 January 2024

Published online: 13 March 2024

 Check for updates

Ranging from subcellular organelle biogenesis to embryo development, the formation of self-organized structures is a hallmark of living systems. Whereas the emergence of ordered spatial patterns in biology is often driven by intricate chemical signalling that coordinates cellular behaviour and differentiation^{1–4}, purely physical interactions can drive the formation of regular biological patterns such as crystalline vortex arrays in suspensions of spermatozoa⁵ and bacteria⁶. Here we discovered a new route to self-organized pattern formation driven by physical interactions, which creates large-scale regular spatial structures with multiscale ordering. Specifically we found that dense bacterial living matter spontaneously developed a lattice of mesoscale, fast-spinning vortices; these vortices each consisted of around 10^4 – 10^5 motile bacterial cells and were arranged in space at greater than centimetre scale and with apparent hexagonal order, whereas individual cells in the vortices moved in coordinated directions with strong polar and vortical order. Single-cell tracking and numerical simulations suggest that the phenomenon is enabled by self-enhanced mobility in the system—that is, the speed of individual cells increasing with cell-generated collective stresses at a given cell density. Stress-induced mobility enhancement and fluidization is prevalent in dense living matter at various scales of length^{7–9}. Our findings demonstrate that self-enhanced mobility offers a simple physical mechanism for pattern formation in living systems and, more generally, in other active matter systems¹⁰ near the boundary of fluid- and solid-like behaviours^{11–17}.

Our work began by investigating the patterns of active turbulence in dense active fluids¹⁸. Active turbulence is characterized by the formation of transient vortices that emerge and disappear randomly. An intriguing question has been whether active turbulence could spontaneously stabilize into ordered spatial structures, despite a number of theoretical predictions^{17,19–21}. To explore such possibility we chose to work with living active fluids consisting of motile bacteria²². We deposited dense suspensions (about 8×10^{10} cells ml^{-1}) of the model flagellated bacterium *Serratia marcescens* (roughly 2 μm in length and 0.8 μm in width) onto the surface of nutrient agar and spread them to create centimetre-scale, quasi-two-dimensional (2D) suspension films of approximate thickness 5–10 μm (Methods). To our surprise we discovered that these quasi-2D dense bacterial suspension films rapidly developed an ordered spatial pattern, at greater than centimetre scale, that was highly stable (Fig. 1a–c, Extended Data Fig. 1 and Supplementary Video 1). This striking pattern consists of mesoscale vortices of uniform size: for example, the vortex diameter shown in Fig. 1a is $278 \pm 51 \mu\text{m}$ (mean \pm s.d., $n = 103$; Methods). The vortices are exclusively clockwise (viewed from above the agar surface; $n > 30$ experiments) and have an average collective speed (Methods) of roughly $24 \mu\text{m s}^{-1}$ (Fig. 1b,c), which is around twofold higher than that outside the vortices (roughly $12 \mu\text{m s}^{-1}$). At the global scale, the pair-correlation function of the vortices shows a pronounced first-order peak corresponding to the average nearest vortex distance (Fig. 1d and Methods) whereas the triplet-distribution function that characterizes the hexagonal

symmetry of a lattice^{5,23} peaked at $\frac{\pi}{3}$, $\frac{2\pi}{3}$ and π (Fig. 1e and Methods). These results show the hexagonal order of the vortex distribution, which is corroborated by anisotropic sixfold symmetry in the 2D spatial correlations of both the collective velocity field (Fig. 1f and Methods) and vorticity field (Extended Data Fig. 2a and Methods).

Hexagonal vortex lattice patterns emerging from active turbulence were previously predicted in theory^{17,19} but never observed experimentally. To further characterize this phenomenon we focused on the scale of individual vortices (Fig. 2a). Using fluorescent cells labelled by genetically encoded green fluorescent protein (GFP), we tracked the motion of single cells in the vortex pattern (Fig. 2b and Methods). Consistent with the results of collective velocity measurement, the mean speed of single cells in the vortices ($24.9 \pm 13.4 \mu\text{m s}^{-1}$; mean \pm s.d., $n > 5,000$) was higher than elsewhere ($14.8 \pm 10.6 \mu\text{m s}^{-1}$; $n > 5,000$; Fig. 2c, top). Interestingly, the motion of cells showed high local polar order within vortices but was disordered outside (Fig. 2c, bottom and Fig. 2d). We noted that cells could travel across vortex boundaries (Fig. 2b) and thus the mechanism of vortex development is different from those arising in spatial confinement²⁴ or due to spatial guidance²⁵. In addition, cell density in the vortices was slightly lower than elsewhere, by about 10–20% (Extended Data Fig. 3 and Methods), which accounts for the variation in vortex brightness seen under phase-contrast microscopy (Fig. 1a). Nonetheless, such density difference is not necessary for vortex formation because some vortex lattice patterns showed similar cell density across vortex boundaries (Extended Data Fig. 3c–e).

¹Department of Physics and Shenzhen Research Institute, The Chinese University of Hong Kong, Shatin, Hong Kong SAR, P.R. China. ✉e-mail: ylwu@cuhk.edu.hk

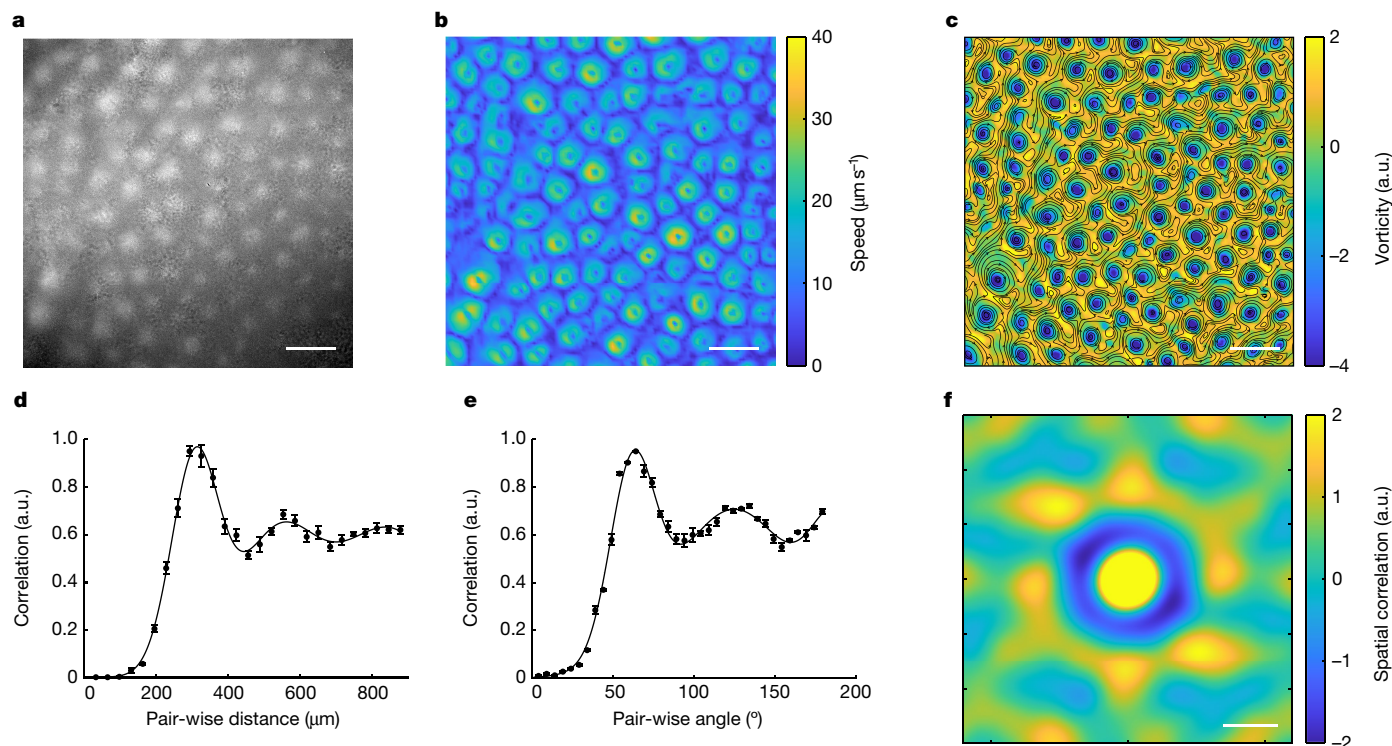


Fig. 1 | Ordered vortex lattice in quasi-2D dense bacterial active fluids.

a, Phase-contrast image of large-scale vortex lattice in a dense suspension of the bacterium *S. marcescens* (roughly 8×10^{10} cells ml^{-1}). **b**, Spatial distribution of time-averaged collective speed for **a** (Methods). **c**, Spatial distribution of time-averaged vorticity for the pattern in **a** (Methods). The value of vorticity indicated by the colour bar is normalized by the mean of absolute vorticity over the entire field. Positive and negative values of vorticity correspond to counterclockwise and clockwise rotation, respectively. Lines ending with an arrow and overlaid on the vorticity colour map indicate flow streamlines of the

collective velocity field (Methods). **b,c**, Data were averaged over a duration of 10 s. The vortex lattice exhibits exclusively clockwise chirality (over 30 experiments) viewed from above the agar plate (that is, viewed through air to the liquid film). **d,e**, Pair-correlation function (**d**) and triplet-distribution function (**e**) of the ordered vortex lattice pattern (Methods). Solid lines were obtained by fitting the data to the sum of three Gaussian functions (Methods). Error bars indicate s.e.m. ($n = 4$). **f**, 2D spatial correlation of the collective velocity field associated with **a** (Methods). Colour bar is in arbitrary units (a.u.). Scale bars, 500 μm (**a-c**), 200 μm (**f**).

We then followed the onset and development dynamics of the ordered vortex lattice (Fig. 3a and Supplementary Video 2). After a short incubation time an initially homogeneous bacterial suspension film showed disordered collective motion reminiscent of bacterial turbulence¹⁸, with transient high-speed streams and irregular vortices emerging at random locations and lasting a few seconds. The lifetime of these transient vortices gradually increased (Fig. 3b) and their shape became more and more regular. Within roughly 5–10 min the vortices became stabilized and settled into a hexagonal lattice pattern. Meanwhile the collective speed of cells (Fig. 3c) shifted from unimodal to bimodal, with cells in vortices having higher collective speed. Notably, the emergence of the ordered vortex lattice required a critical cell density of approximately $5.5 \times 10^{10} \text{ ml}^{-1}$ (Fig. 3d,e); below this critical cell density the bacterial suspension showed active turbulence only (Extended Data Fig. 4).

In summary, the dense bacterial active fluid spontaneously developed a large-scale vortex lattice pattern with multiscale ordering. We note that this phenomenon does not involve cell-secreted polymers such as extracellular DNA and amyloid fibres (Methods), which have been shown to promote large-scale self-organization in dense bacterial active matter^{26,27}. The phenomenon appears to require a sufficiently high cell motility. Indeed, when we reduced the motility of *S. marcescens* by around 50% using violet light illumination (Extended Data Fig. 5 and Methods)²⁷ most vortices in the large-scale vortex lattice dissolved, leaving few in the field of view (Supplementary Video 3); meanwhile, the bimodal distribution of collective speed relaxed to unimodal (Fig. 3f). Moreover, the formation of similar mesoscale vortices was observed with *Escherichia coli* (Extended Data Fig. 6a,b, Supplementary Video 4 and Methods). However, the numbers of vortices that emerged in a

suspension film of *E. coli* were sporadic (typically fewer than ten in a field of about 10 mm^2) and disordered, presumably due to the lower motility of *E. coli* cells (Extended Data Fig. 6b).

What then is the origin of the ordered vortex lattice pattern? Before answering this question we first sought to understand why individual cells in the vortices moved at higher speed (Fig. 2c, top) despite the fact that all cells in the bacterial suspension should have had a similar self-propulsion force because they were prepared from a homogeneous culture (Extended Data Fig. 5b). This suggests that the vortex physical environment is different from that elsewhere. We reasoned that the higher polar order of cellular motion in the vortices allows a coherent group of cells to generate a stronger local collective active stress²⁸, which would modify the local mechanical environment and result in higher active transport for cells in the friction-dominated quasi-2D suspension film^{26,29}. To examine this idea we measured the relation between apparent single-cell speed (denoted as v) and local polar order (denoted as $P = |\sum_i \mathbf{p}_i|/n$, where n is the total number of cells near a cell of interest and \mathbf{p}_i represents the polarization of cell i among n cells); P serves as a proxy for the magnitude of local collective active stress, σ , because $-\nabla \cdot \sigma = \sum_i \mathcal{F}_i$ (ref. 28), where \mathcal{F}_i is the active force density generated by cell i and $\mathcal{F}_i \propto \mathbf{p}_i$. Indeed, we found that v increases with P and that the relation can be fitted by the linear relation $v = \gamma_0(1 + \beta P)$, with β being a positive dimensionless coefficient and γ_0 the average speed of cells in the disordered phase with $P = 0$ (Fig. 4a). Interestingly, coefficient β increases with cell density and its approximate value can be as high as 1.7 (Fig. 4b). Denoting the self-propulsion force of cells as f_0 and the single-cell mobility coefficient as μ , we have $v = \mu f_0$ and the above linear relation implying the single-cell mobility coefficient

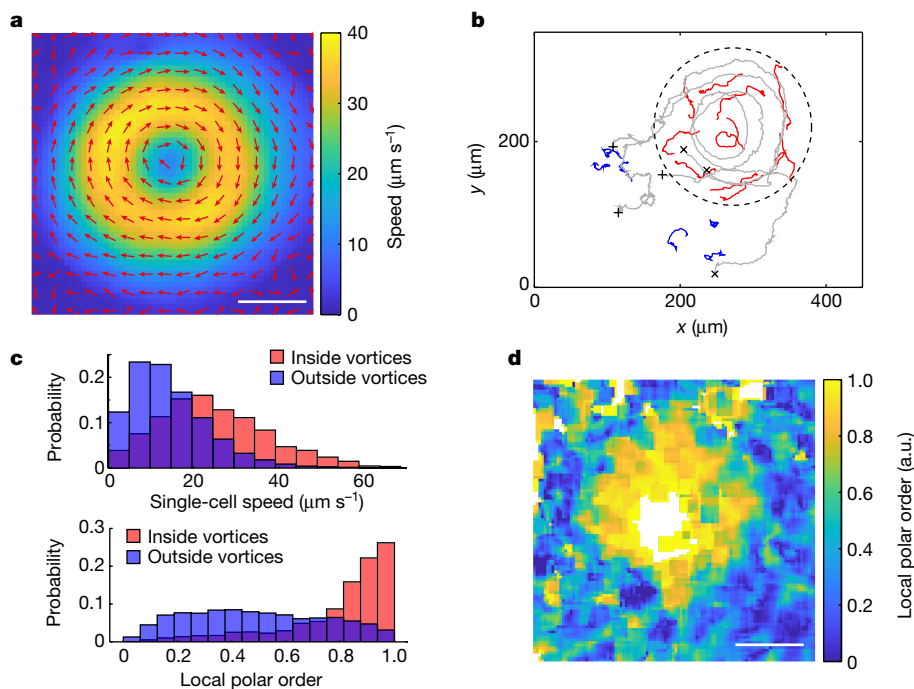


Fig. 2 | Microscale characteristics of the ordered vortex lattice. **a**, Time-averaged collective velocity field of a single vortex in the lattice (Methods). Data were averaged over a duration of 10 s. Arrows and colour map represent collective velocity direction and magnitude, respectively. **b**, Representative single-cell trajectories near a vortex in the lattice. Red and blue lines show the trajectories (lasting for 5 s) inside and outside the vortex, respectively, with the vortex boundary indicated by the dashed line; grey lines represent the trajectories

(lasting for 25 s) of cells travelling across the vortex boundary (+, starting points; ×, ending points). **c**, Probability distributions of single-cell speed (top) and local polar order of single-cell motion (bottom) in the vortex lattice. The overlap of the red and blue histograms is shown in purple. **d**, Spatial distribution of local polar order near the vortex associated with **b** (Methods). Scale bars, 100 μm.

$\mu \propto (1 + \beta P)$, which supports the notion that collective active stress in dense bacterial suspensions enhances cell mobility. We term this behaviour self-enhanced mobility—that is, the speed of individual cells increases with cell-generated collective stresses while holding cell density constant. In this respect, mobility refers to the ability of cells to move under the mechanical constraints of their surroundings; by contrast, motility is the intrinsic self-propulsion speed of cells in an isolated environment, as measured in Extended Data Fig. 5b.

The self-enhanced mobility of bacteria in dense suspensions was implied in the nonlinear positive relation between local polar order and collective speed in earlier studies on the so-called zooming biometric phase phenomenon^{30,31}; here our results based on single-cell speed measurement provide insight into this phenomenon. The behaviour of self-enhanced mobility does not necessarily imply that the apparent speed of individual cells is higher than that of isolated cells at zero-density limit, because the average speed of cells in the disordered phase (that is, v_0 in the speed-order relation $v = v_0(1 + \beta P)$) is inversely correlated with cell density. In addition it should be distinguished from the macroscopic viscosity reduction observed in semidilute bacterial suspensions^{32,33}; the latter arises from the onset of collective motion of cells under weak external shear, with single-cell speed remaining constant³⁴.

Self-enhanced mobility in dense bacterial suspensions offers a potential mechanism to explain the emergence of mesoscale vortices. Spontaneous fluctuations in dense bacterial suspensions could give rise to domains with higher polar order (and hence with higher collective stress); such domains, with higher speed and longer persistence time than less-ordered domains, could recruit nearby cells via polar alignment interactions and grow in size until cell recruitment is balanced by cell loss, eventually developing into stable vortices. To examine this hypothesis we developed a Vicsek-type particle-based model³⁵ (Methods). Each bacterial cell i is modelled as an active Brownian particle that propels

itself in 2D space with variable mobility $\mu_i \equiv v_i/f_i$ (v_i and f_i are particle speed and self-propulsion force, respectively) and that depends on local polar order (denoted as P_i) in the form $\mu_i \propto (1 + \beta P_i)$ ($\beta \geq 0$); here β corresponds to the dimensionless coefficient in the experimental relation $v \propto (1 + \beta P)$, and henceforth is referred to as the mobility enhancement coefficient.

Numerical simulation of the particle-based model showed that the emergent dynamics of the system depend on mobility enhancement coefficient β and particle activity (that is, ensemble average of particle self-propulsion force $f_0 = \langle f_i \rangle$, proportional to single-cell motility measured in experiments such as those shown in Extended Data Fig. 5b). As shown in the phase map in Fig. 4c, the system develops a stable vortex lattice pattern at sufficiently large β and f_0 (Fig. 4d,e, Extended Data Figs. 7–9 and Supplementary Video 5). The stable vortex pattern shows features similar to those of the large-scale vortex lattice observed experimentally (Extended Data Figs. 7 and 9). At small β (for example, $\beta < 0.5$ for intermediate $f_0 = 10$), the model produces a disordered state without stable vortices, similar to the experimental phenomenon observed below critical cell density for the development of vortex lattices (Extended Data Fig. 4). It is important to note that the mechanism of self-enhanced mobility is essential, because the system cannot develop stable vortices in the absence of mobility enhancement (that is, $\beta = 0$); particles in the model tend to move in curved trajectories but this is insufficient to form stable vortices via polar alignment, although this tendency appears to control the size of vortices (Extended Data Fig. 9k and Methods). These results support the notion that self-enhanced mobility underlies the onset of the vortex lattice pattern in dense bacterial suspensions (Supplementary Information).

Although the particle-based model can reproduce the formation of a vortex lattice pattern, the hexagonal order of the vortex pattern is weaker compared with that observed experimentally (Extended Data Fig. 8a). This is probably due to the absence of hydrodynamic

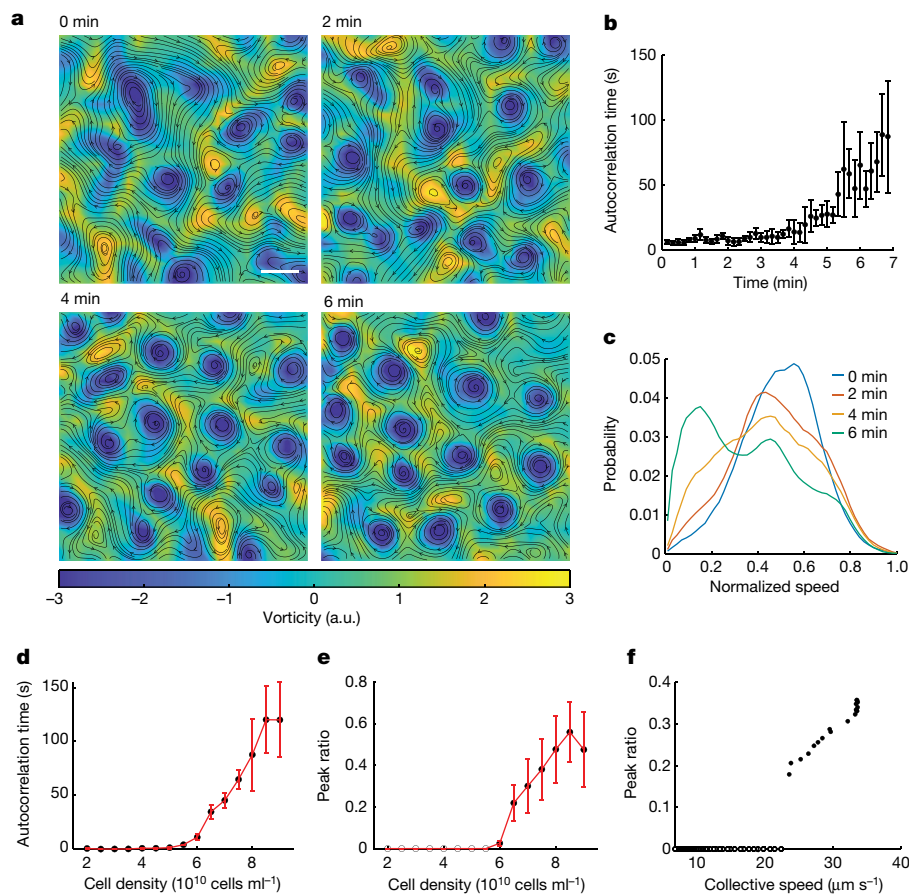


Fig. 3 | Emergence of ordered vortex lattice. **a**, Time sequence of instantaneous vorticity field during the emergence of an ordered vortex lattice in a dense bacterial suspension (roughly 8×10^{10} cells ml^{-1}). The vorticity field was plotted in the same manner as in Fig. 1c. **b**, Transient autocorrelation time of collective velocity (as a measure of vortex lifetime) during the developmental process of the vortex lattice shown in **a** (Methods). Error bars indicate s.e.m. ($n \geq 9$; Methods). **c**, Probability distributions of normalized collective speed during the developmental process shown in **a**. Colours represent the time elapsed. **d, e**, Steady-state autocorrelation time of collective velocity (**d**) and peak ratio in collective speed distribution (**e**) plotted against cell density. Peak ratio is defined as the ratio

between the height of the higher-speed peak (corresponding to the vortex region) and the lower-speed peak in the collective speed distribution, as shown in **c** (Methods). **e**, Filled circles represent data from bimodal speed distributions, with empty circles corresponding to zero peak ratio and representing data from unimodal speed distributions (the higher-speed peak has a height of zero). **f**, Peak ratio in collective speed distribution plotted against the average collective speed of cells (cell density around 8×10^{10} ml^{-1}). Here the average collective speed serves as a proxy for single-cell motility (Extended Data Fig. 5), which was tuned by violet light illumination (Methods). Scale bar, 200 μm .

interaction between vortices that could reorganize their spatial distribution. To account for the effect of hydrodynamic interaction during vortex lattice development we adopted the framework of a minimal continuum model based on the seminal Toner–Tu active fluids model³⁶ and a Swift–Hohenberg-type fourth-order term²⁹ that successfully describes active turbulence in dense bacterial suspensions^{18,19,37} (Methods). A new key ingredient in our model is that, to account for the behaviour of self-enhanced mobility, effective viscosity η_{eff} (which is inversely proportional to single-cell mobility) entering the model parameters³⁸ is taken as being dependent on local polar order P as $\eta_{\text{eff}} \propto 1/(1 + \beta P)$; here β corresponds to the mobility enhancement coefficient described above experimentally and in particle-based modelling (Methods). As shown in the phase map in Fig. 4f, numerical simulations of the continuum model produce a large-scale crystalline vortex lattice with hexagonal order and uniform chirality at strong mobility enhancement and high activity (denoted by activity parameter $|S|$; $S < 0$ for pusher-type swimmers such as *S. marcescens*¹⁸; Fig. 4g, h, Extended Data Figs. 8–10 and Supplementary Video 6). By contrast, the model produces active turbulence at weak mobility enhancement and low activity (Extended Data Fig. 10a, b). These results are consistent with experimental and particle-based simulations. We note that, for sufficiently large activity $|S|$, the original model lacking self-enhanced

mobility (equivalent to $\beta = 0$ in our simulation) was shown to produce hexagonal vortex lattices owing to nonlinear energy transfer¹⁷. However, because our numerical simulations were performed in the regime of S that would have led to the active turbulence state in the absence of self-enhanced mobility (Fig. 4f), vortex lattice development enabled by self-enhanced mobility, as studied here, arises via a different pathway despite having similar phenomenology¹⁷.

Taken together, we have discovered that self-enhanced mobility in dense bacterial suspensions creates multiscale spatial order out of active turbulence, driving the formation of mesoscale vortices arranged in a centimetre-scale hexagonal lattice. The vortex lattice pattern studied here is different from several examples previously reported^{5,6,39–41}, in regard to both the phenomenology and underlying mechanism (Supplementary Information). Vortex structures are characteristic of turbulent flows that are ubiquitous in nature spanning vast length scales, ranging from quantum fluids to galaxies. Here we demonstrate a unique route by which chaotic vortex structures in turbulent flows can spontaneously stabilize. Ordered vortex structures have long been theoretically predicted in dense active polar fluids^{17,19,29,42,43}, and our work provides experimental evidence.

More generally, our work suggests self-enhanced mobility as a generic mechanism for self-organization in dense living matter and

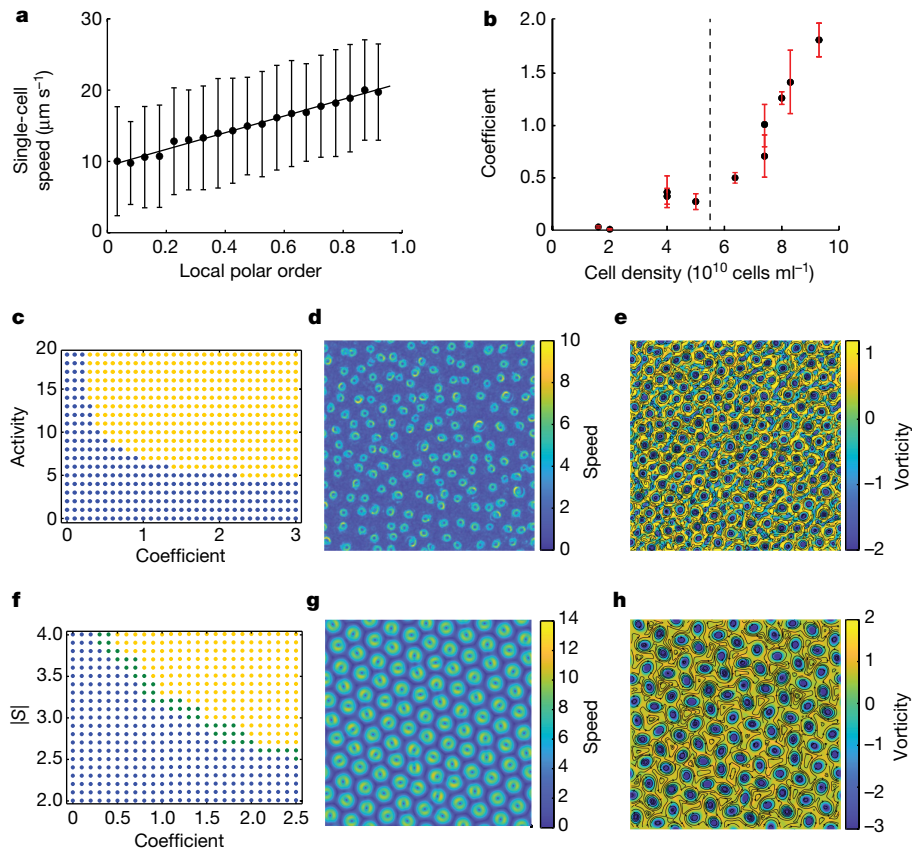


Fig. 4 | Self-enhanced mobility in dense bacterial suspensions underlies the formation of ordered vortex lattices. **a**, Apparent single-cell speed obtained by single-cell tracking plotted against local polar order in dense bacterial active fluids showing ordered vortex lattices (cell density approximately $8 \times 10^{10} \text{ ml}^{-1}$; Methods). Solid line is a linear fit to the data in the form of $v \propto (1 + \beta P)$, with the dimensionless coefficient β being 1.25 ± 0.12 ; error bars represent s.d. ($n > 500$ single-cell trajectory segments for each data point). **b**, Coefficient β in the experimental relation $v \propto (1 + \beta P)$ plotted against cell density. Dashed line indicates minimal cell density for the development of ordered vortex lattices. Error bars represent fitting error of β . **c**, Phase diagram of emergent collective motion patterns in particle-based simulations plotted in the plane of mobility enhancement coefficient β and particle activity f_0 (yellow dots, vortex lattice; blue dots, active turbulence). **d,e**, Spatial distributions of time-averaged

collective speed (**d**) and vorticity (**e**) in the vortex lattice pattern produced in a representative particle-based simulation at steady state (Methods). Data were averaged over a duration of 100 time units and plotted in the same manner as in Fig. 1b,c. Simulation parameters $f_0 = 10$ and $\beta = 1.2$. **f**, Phase diagram of emergent collective motion patterns in continuum modelling plotted in the plane of mobility enhancement coefficient β and activity $|S|$ (yellow, hexagonal vortex lattice; blue, active turbulence; green, coexistence of hexagonal vortex lattice and active turbulence). **g,h**, Spatial distribution of time-averaged collective speed $|v|$ (**g**) and vorticity ω (**h**) in the vortex lattice pattern produced in a representative continuum simulation at steady state. Data were averaged over a duration of ten time units and plotted as in Fig. 1b,c. Simulation parameters $|S| = 3.5$ and $\beta = 2.0$.

synthetic active matter⁴⁴. In this mechanism, mobility enhancement could be due to either modification of the local physical environment by self-generated mechanical stresses (via motility or growth) or active regulation of motility in response to local stimuli. The mechanism may therefore provide new insights into large-scale cell movement in the developing animal embryo^{45,46}. Meanwhile, active fluids share phenomenological similarities with quantum superfluids⁴⁷. Our findings may offer a new perspective to examine the analogy between active and quantum fluids.

Online content

Any methods, additional references, Nature Portfolio reporting summaries, source data, extended data, supplementary information, acknowledgements, peer review information; details of author contributions and competing interests; and statements of data and code availability are available at <https://doi.org/10.1038/s41586-024-07114-8>.

1. Murray, J. D. *Mathematical Biology: I. An Introduction* (Springer, 2007).
2. Budrene, E. O. & Berg, H. C. Complex patterns formed by motile cells of *Escherichia coli*. *Nature* **349**, 630–633 (1991).

3. Kessler, D. A. & Levine, H. Pattern formation in *Dictyostelium* via the dynamics of cooperative biological entities. *Phys. Rev. E* **48**, 4801 (1993).
4. Liu, C. et al. Sequential establishment of stripe patterns in an expanding cell population. *Science* **334**, 238–241 (2011).
5. Riedel, I. H., Kruse, K. & Howard, J. A self-organized vortex array of hydrodynamically entrained sperm cells. *Science* **309**, 300–303 (2005).
6. Petroff, A. P., Wu, X.-L. & Libchaber, A. Fast-moving bacteria self-organize into active two-dimensional crystals of rotating cells. *Phys. Rev. Lett.* **114**, 158102 (2015).
7. Mongera, A. et al. A fluid-to-solid jamming transition underlies vertebrate body axis elongation. *Nature* **561**, 401–405 (2018).
8. Qin, B. et al. Cell position fates and collective fountain flow in bacterial biofilms revealed by light-sheet microscopy. *Science* **369**, 71–77 (2020).
9. Parry, B. R. et al. The bacterial cytoplasm has glass-like properties and is fluidized by metabolic activity. *Cell* **156**, 183–194 (2014).
10. Marchetti, M. C. et al. Hydrodynamics of soft active matter. *Rev. Mod. Phys.* **85**, 1143–1189 (2013).
11. Angelini, T. E. et al. Glass-like dynamics of collective cell migration. *Proc. Natl Acad. Sci. USA* **108**, 4714–4719 (2011).
12. Delarue, M. et al. Self-driven jamming in growing microbial populations. *Nat. Phys.* **12**, 762–766 (2016).
13. Geyer, D., Martin, D., Tailleur, J. & Bartolo, D. Freezing a flock: motility-induced phase separation in polar active liquids. *Phys. Rev.* **9**, 031043 (2019).
14. Henkes, S., Fily, Y. & Marchetti, M. C. Active jamming: self-propelled soft particles at high density. *Phys. Rev. E* **84**, 040301 (2011).
15. Bi, D., Lopez, J. H., Schwarz, J. M. & Manning, M. L. A density-independent rigidity transition in biological tissues. *Nat. Phys.* **11**, 1074–1079 (2015).
16. Mandal, R., Bhuyan, P. J., Chaudhuri, P., Dasgupta, C. & Rao, M. Extreme active matter at high densities. *Nat. Commun.* **11**, 2581 (2020).

17. James, M., Suchla, D. A., Dunkel, J. & Wilczek, M. Emergence and melting of active vortex crystals. *Nat. Commun.* **12**, 5630 (2021).
18. Wensink, H. H. et al. Meso-scale turbulence in living fluids. *Proc. Natl Acad. Sci. USA* **109**, 14308–14313 (2012).
19. Dunkel, J., Heidenreich, S., Bär, M. & Goldstein, R. E. Minimal continuum theories of structure formation in dense active fluids. *New J. Phys.* **15**, 045016 (2013).
20. Reinken, H., Heidenreich, S., Bär, M. & Klapp, S. H. L. Anisotropic mesoscale turbulence and pattern formation in microswimmer suspensions induced by orienting external fields. *New J. Phys.* **21**, 013037 (2019).
21. Doostmohammadi, A., Adamer, M. F., Thampi, S. P. & Yeomans, J. M. Stabilization of active matter by flow-vortex lattices and defect ordering. *Nat. Commun.* **7**, 10557 (2016).
22. Aranson, I. Bacterial active matter. *Rep. Prog. Phys.* **85**, 076601 (2022).
23. Zahn, K., Maret, G., Ruß, C. & von Grünberg, H. H. Three-particle correlations in simple liquids. *Phys. Rev. Lett.* **91**, 115502 (2003).
24. Wioland, H., Woodhouse, F. G., Dunkel, J., Kessler, J. O. & Goldstein, R. E. Confinement stabilizes a bacterial suspension into a spiral vortex. *Phys. Rev. Lett.* **110**, 268102 (2013).
25. Nishiguchi, D., Aranson, I. S., Snezhko, A. & Sokolov, A. Engineering bacterial vortex lattice via direct laser lithography. *Nat. Commun.* **9**, 4486 (2018).
26. Liu, S., Shankar, S., Marchetti, M. C. & Wu, Y. Viscoelastic control of spatiotemporal order in bacterial active matter. *Nature* **590**, 80–84 (2021).
27. Xu, H., Huang, Y., Zhang, R. & Wu, Y. Autonomous waves and global motion modes in living active solids. *Nat. Phys.* **19**, 46–51 (2023).
28. Ramaswamy, S. The mechanics and statistics of active matter. *Annu. Rev. Condens. Matter Phys.* **1**, 323–345 (2010).
29. Oza, A. U., Heidenreich, S. & Dunkel, J. Generalized Swift-Hohenberg models for dense active suspensions. *Eur. Phys. J. E* **39**, 97 (2016).
30. Cisneros, L. H., Cortez, R., Dombrowski, C., Goldstein, R. E. & Kessler, J. O. Fluid dynamics of self-propelled microorganisms, from individuals to concentrated populations. *Exp. Fluids* **43**, 737–753 (2007).
31. Cisneros, L. H., Kessler, J. O., Ganguly, S. & Goldstein, R. E. Dynamics of swimming bacteria: transition to directional order at high concentration. *Phys. Rev. E* **83**, 061907 (2011).
32. Sokolov, A. & Aranson, I. S. Reduction of viscosity in suspension of swimming bacteria. *Phys. Rev. Lett.* **103**, 148101 (2009).
33. López, H. M., Gachelin, J., Douarache, C., Auradou, H. & Clément, E. Turning bacteria suspensions into superfluids. *Phys. Rev. Lett.* **115**, 028301 (2015).
34. Martínez, V. A. et al. A combined rheometry and imaging study of viscosity reduction in bacterial suspensions. *Proc. Natl Acad. Sci. USA* **117**, 2326–2331 (2020).
35. Vicsek, T., Czirók, A., Ben-Jacob, E., Cohen, I. & Shochet, O. Novel type phase transition in a system of self-driven particles. *Phys. Rev. Lett.* **75**, 1226–1229 (1995).
36. Toner, J., Tu, Y. & Ramaswamy, S. Hydrodynamics and phases of flocks. *Ann. Phys.* **318**, 170–244 (2005).
37. Dunkel, J. et al. Fluid dynamics of bacterial turbulence. *Phys. Rev. Lett.* **110**, 228102 (2013).
38. Heidenreich, S., Dunkel, J., Klapp, S. H. & Bär, M. Hydrodynamic length-scale selection in microswimmer suspensions. *Phys. Rev. E* **94**, 020601 (2016).
39. Sumino, Y. et al. Large-scale vortex lattice emerging from collectively moving microtubules. *Nature* **483**, 448–452 (2012).
40. Nakane, D., Odaka, S., Suzuki, K. & Nishizaka, T. Large-scale vortices with dynamic rotation emerged from monolayer collective motion of gliding *Flavobacteria*. *J. Bacteriol.* **203**, e0007321 (2021).
41. Patra, P. et al. Collective migration reveals mechanical flexibility of malaria parasites. *Nat. Phys.* **18**, 586–594 (2022).
42. Supekar, R. et al. Learning hydrodynamic equations for active matter from particle simulations and experiments. *Proc. Natl Acad. Sci. USA* **120**, e2206994120 (2023).
43. James, M., Bos, W. J. & Wilczek, M. Turbulence and turbulent pattern formation in a minimal model for active fluids. *Phys. Rev. Fluids* **3**, 061101 (2018).
44. Yan, J. et al. Reconfiguring active particles by electrostatic imbalance. *Nat. Mater.* **15**, 1095 (2016).
45. Jacobson, A. G. Somitomeres: mesodermal segments of vertebrate embryos. *Development* **104**, 209–220 (1988).
46. Voiculescu, O., Bertocchini, F., Wolpert, L., Keller, R. E. & Stern, C. D. The amniote primitive streak is defined by epithelial cell intercalation before gastrulation. *Nature* **449**, 1049–1052 (2007).
47. Słomka, J. & Dunkel, J. Geometry-dependent viscosity reduction in sheared active fluids. *Phys. Rev. Fluids* **2**, 043102 (2017).

Publisher's note Springer Nature remains neutral with regard to jurisdictional claims in published maps and institutional affiliations.

Springer Nature or its licensor (e.g. a society or other partner) holds exclusive rights to this article under a publishing agreement with the author(s) or other rightsholder(s); author self-archiving of the accepted manuscript version of this article is solely governed by the terms of such publishing agreement and applicable law.

© The Author(s), under exclusive licence to Springer Nature Limited 2024

Methods

Bacterial strains

The following strains were used: wild-type *S. marcescens* ATCC 274; *S. marcescens* GFP (*S. marcescens* ATCC 274 with constitutive expression of GFP encoded on the plasmid pAM06-tet⁴⁸ (from A. Mukherjee and C. M. Schroeder, University of Illinois at Urbana-Champaign); *E. coli* HCB1737 (a derivative of *E. coli* AW405 with wild-type flagellar motility (from H. Berg, Harvard University); and *E. coli* GFP (*E. coli* HCB1737 hosting the plasmid pAM06-tet). Plasmids were transformed into strains by electroporation. Single-colony isolates were grown overnight (about 13–14 h) with shaking in lysogeny broth medium (1% Bacto Tryptone, 0.5% yeast extract, 0.5% NaCl) at 30 °C to stationary phase. For *S. marcescens* GFP and *E. coli* GFP, kanamycin (50 µg ml⁻¹) was added to the growth medium for plasmid maintenance.

Agar plates

Lysogeny broth agar (0.6% Difco Bacto agar infused with 1% Bacto Tryptone, 0.5% yeast extract and 0.5% NaCl; all concentrations reported as wt/vol) was autoclaved and stored at room temperature. Before use the agar was melted in a microwave oven, cooled to around 60 °C and pipetted in 10 ml aliquots into non-vented 90 mm polystyrene Petri plates. For exclusion of cell-secreted polymers, including extracellular DNA and amyloid fibres, agar plates were supplemented by DNase I (200 U ml⁻¹; Thermo Fisher, catalogue no. 18047019) and proteinase K (greater than 12 mAU ml⁻¹; QIAamp DNA Mini Kit 50, Qiagen, catalogue no. 51304). Plates were swirled gently to ensure surface flatness, cooled for 10 min without a lid inside a large Plexiglas box and then covered by the lid for further experiments.

Fabrication of quasi-2D bacterial suspension films

Highly motile cells were collected from overnight bacterial cultures, washed by centrifugation and resuspended to the desired cell densities in fresh medium. Next, 20 µl of resuspended bacterial culture was deposited on a fresh 0.6% agar plate (as described above). Following deposition the dense bacterial suspension expanded and eventually became a quasi-2D suspension film of approximate diameter 3–4 cm and approximate thickness 5–10 µm, except at the centre and very near the edge (where thickness was tens of microns). Therefore, the quasi-2D dense bacterial suspension film was in contact with a solid substrate (bottom) and had a free air–liquid interface (top), with the side boundary of the suspension film being a three-phase air–liquid–solid interface. The observation window for quantitative measurements in the vortex pattern is typically less than 3.3 × 3.3 mm² and the centre of the observation window is about 1 cm away from the centre or edge of the suspension film.

For assessment of bacterial density the quasi-2D bacterial suspension film as prepared consisted entirely of GFP-tagged cells; to track the motion of single cells, the bacterial suspension consisted of a mixture of GFP-tagged and wild-type cells at 1:2,000. The agar plate with the prepared quasi-2D bacterial suspension film was first incubated at 30 °C in a custom-built plate-imaging box, allowing cell motility to adapt to the surface environment; as soon as large-scale patterns appeared the plate was transferred to the microscope stage for further imaging. The diameter of vortices in the vortex lattice pattern is uniform for a specific sample but may vary across different experiments, ranging from around 300 to 400 µm. The rotation chirality of the vortices was exclusively clockwise (viewed from above the agar plate), consistent with the rotation bias of isolated bacteria moving near the agar substrate (Extended Data Fig. 2b).

Microscopy imaging

All imaging was performed on a motorized inverted microscope (Nikon TI-E). Phase-contrast images were acquired with either a ×4, ×10 or ×20 objective and recorded by a scientific complementary

metal-oxide-semiconductor camera (Andor Zyla 4.2 PLUS USB 3.0) at 30 or 10 fps (to record the onset and development of the vortex lattices) and at full-frame size (2,048 × 2,048 pixels). For assessment of bacterial density or to track the motion of individual bacteria, GFP-tagged bacterial cells were imaged in epifluorescence using the ×20 objective and a fluorescein isothiocyanate (FITC) filter cube (excitation 482/35 nm, emission 536/40 nm, dichroic 506 nm; Semrock, Inc.), with the excitation light provided by a mercury precentred fibre illuminator (Nikon Intensilight; fluorescence images were recorded with the scientific complementary metal-oxide-semiconductor camera described above at full-frame size and 10 fps (exposure time 90 ms for cell density measurement and 40 ms for single-cell tracking). In all experiments the camera was controlled by NIS Elements (Nikon). When acquiring fluorescence images for single-cell tracking, phase-contrast images of the bacterial suspension film were acquired simultaneously. To tune the motility of cells in the bacterial suspension films, cells were illuminated by violet light of approximate intensity 1,688 mW cm⁻² provided by the Nikon Intensilight, then passaged through the ×10 objective via a 406 nm filter (406/15 nm; FF01-406/15-25, Semrock, Inc.). In all experiments the Petri dishes were covered with a lid to prevent evaporation and air convection. Sample temperature was maintained at 30 °C via a custom-built temperature-control system installed on the microscope stage.

Experimental image processing and data analysis

Microscopy images were processed using open-source Fiji (ImageJ) software (<http://fiji.sc/Fiji>) and custom-written programs in MATLAB (The MathWorks). For computation of collective velocity field in quasi-2D bacterial suspension films we performed particle image velocimetry (PIV) analysis based on phase-contrast time-lapse videos using open-source package MatPIV 1.6.1 written by J. K. Sveen (<http://folk.uio.no/jks/matpiv/index2.html>). For each pair of consecutive images obtained with the ×4, ×10 or ×20 objective, PIV interrogation-window size began at either 104 × 104, 41.6 × 41.6 or 20.8 × 20.8 µm² and ended at either 26 × 26, 10.4 × 10.4 or 5.2 × 5.2 µm², respectively, following three iterations; the grid size of the resulting velocity field was either 13 × 13, 5.2 × 5.2 or 2.6 × 2.6 µm², respectively. Before processing, microscopy images were smoothed to reduce noise by convolution with a Gaussian kernel of approximate standard deviation 1 µm. The results were insensitive to variation in the parameters of smoothing and interrogation window size. PIV analysis yielded space- and time-dependent collective velocity field $\mathbf{v}(\mathbf{r}, t) = (v_x, v_y)$ and vorticity field $\omega(\mathbf{r}, t) = \partial_x v_y - \partial_y v_x$. The magnitude of $\mathbf{v}(\mathbf{r}, t)$ is taken as the collective speed. Positive and negative values of $\omega(\mathbf{r}, t)$ correspond to counter-clockwise and clockwise rotation, respectively. For visualization of the collective velocity or vorticity field as computed by PIV analysis, the field was coarse grained and plotted on a square mesh with appropriate grid spacing. Flow streamlines were computed by the built-in streamslice function in MATLAB and plotted on the vorticity field.

For identification of the position of vortex centres and calculation of vortex diameter, vortices that emerged in quasi-2D bacterial suspension films in a specific image frame were first segmented by the criterion $\omega(\mathbf{r}) < -(|\omega(\mathbf{r})|)_\rho/2$, where the angular bracket represents averaging over \mathbf{r} . The segmented vortices consist of isolated domains, each representing a single vortex and with its centre taken as the position of vortex centre \mathbf{r}_α ($\alpha = 1, 2, 3, \dots$ is the index of the vortices).

These vortex centre positions, \mathbf{r}_α , were used to calculate the pair-correlation function (Fig. 1d) and triplet-distribution function^{5,23} (Fig. 1e). The pair-correlation function is defined as $g(r) = \frac{1}{2\pi\rho} \sum_{\alpha \neq \beta} \delta(r - |\mathbf{r}_\beta - \mathbf{r}_\alpha|)$, where ρ is vortex number density (here we assumed that vortex distribution is translation invariant). The triplet-distribution function is defined as $g(\phi) = \frac{1}{N} \sum_{(\beta, \gamma) \neq \alpha} \delta[\theta(\mathbf{r}_\beta - \mathbf{r}_\alpha, \mathbf{r}_\gamma - \mathbf{r}_\alpha) - \phi]$, where vortex β and γ are two different nearest vortices of vortex α and $\theta(\mathbf{a}, \mathbf{b})$ represents the angle between vectors \mathbf{a} and \mathbf{b} . The nearest vortices were recognized via the Voronoi tessellation approach. The pair-correlation and triplet-distribution functions were fitted into the sum of Gaussian

Article

functions (the number is chosen to match the number of peaks). For further quantification of the spatial order of vortices, the 2D spatial autocorrelation of the collective velocity field (Fig. 1f) and vorticity field (Extended Data Fig. 2a) was calculated by $C_v(\Delta\mathbf{r}) = \langle \frac{\mathbf{v}(\mathbf{r}) \times \mathbf{v}(\mathbf{r} + \Delta\mathbf{r})}{|\mathbf{v}(\mathbf{r})|^2} \rangle_{\mathbf{r}}$ and $C_\omega(\Delta\mathbf{r}) = \langle \frac{\omega(\mathbf{r})\omega(\mathbf{r} + \Delta\mathbf{r})}{|\omega(\mathbf{r})|^2} \rangle_{\mathbf{r}}$, respectively, where the angular brackets represent averaging over \mathbf{r} .

The trajectories of bacterial cells were obtained by single-cell tracking based on the recorded fluorescence videos using a custom-written program in MATLAB⁴⁹. Cell positions, $\mathbf{r}_i(t)$ ($i = 1, 2, 3, \dots$ is the index of the tracked cells) and swimming velocity, $\mathbf{v}_i(t)$, were computed based on the trajectories. Instantaneous single-cell speed (Fig. 4a) was computed every 20 ms, which is much shorter than cell trajectory persistence time ($\tau = 0.58 \pm 0.23$ s inside vortices and $\tau = 0.36 \pm 0.22$ s outside; mean \pm s.d., $n = 100$ cells). The steady-state local polar order of tracked single cells located near position \mathbf{r} , as shown in Fig. 2d, is defined as $P(\mathbf{r}) = |\langle \mathbf{n}_i \rangle_{i,t}|$, where $\mathbf{n}_i = \mathbf{v}_i/|\mathbf{v}_i|$ is velocity direction with the angular bracket representing averaging over both cell index i , whose position \mathbf{r}_i satisfies $|\mathbf{r} - \mathbf{r}_i| \leq 6.5 \mu\text{m}$, and the entire time window of cell tracking. Because single-cell tracking is of low throughput due to the trade-off between tracking precision and density of cells being tracked, we computed instantaneous local polar order $P(\vec{r}, t)$ based on local collective velocity field measured by PIV as $P(\vec{r}, t) = |\langle \mathbf{v}(\mathbf{r}', t)/|\mathbf{v}(\mathbf{r}', t)| \rangle_{\mathbf{r}'}|$, where the angular bracket represents averaging over PIV-derived velocity vectors at \mathbf{r}' that satisfies $|\mathbf{r} - \mathbf{r}'| \leq 6.5 \mu\text{m}$.

To quantify the lifetime of vortices during the development of vortex lattices we first computed the transient autocorrelation function of the collective velocity field at a specific time, T , defined as $C(T, \Delta t) = \frac{\langle \mathbf{v}(\mathbf{r}, T) \times \mathbf{v}(\mathbf{r}, T + \Delta t) \rangle_{\mathbf{r}, T}}{\langle |\mathbf{v}(\mathbf{r}, T)|^2 \rangle_{\mathbf{r}, T}}$, where the angular brackets represent both spatial averaging over the entire collective velocity field and averaging over time t that satisfies $0 \leq t - T \leq 10$ s. $C(T, \Delta t)$ was then fitted to exponential function $C(T, \Delta t) \propto e^{-\Delta t/\tau_0}$, where τ_0 represents the transient autocorrelation time at time T as shown in Fig. 3b.

For calculation of peak ratio in the collective speed distribution shown in Fig. 3e, f and Extended Data Fig. 9, collective speed distribution in experiments or simulations was first smoothed via a Gaussian filter (imgaussfilt function in MATLAB). Peaks were identified via the built-in findpeaks function in MATLAB, with peak ratio defined as the ratio between the height of the higher-speed peak (corresponding to the vortex region) and that of the lower-speed peak in collective speed distribution.

Particle-based simulation and data analysis

In the simulations we considered a collective of overdamped, self-propelled particles moving in 2D space. Specifically, for the i -th particle its self-propulsion speed is given by $v_i = \mu_i f_i$, where μ_i is the effective mobility coefficient of the particle and f_i is the self-propulsion force. The mobility μ_i follows a linear relation with the local polar order in the vicinity of particle i (denoted as P_i) in the form of $\mu_i \propto (1 + \beta P_i)$; here $\beta \geq 0$ is the dimensionless mobility enhancement coefficient. In addition, the model accommodates steric and hydrodynamic interactions between swimmers as effective coupling of particle orientation and angular velocity, in a way similar to that adopted earlier to simulate the collective motion of millions of cells in large-scale dense bacterial active fluids⁵⁰. The dynamics of the i -th particle in terms of its centre of mass position \mathbf{r}_i , orientation θ_i and angular velocity ω_i are governed by the following equations:

$$\dot{\mathbf{r}}_i = \mu_i f_i \hat{\mathbf{n}}_i + \sqrt{2D_r} \xi_r, \quad (1)$$

$$\dot{\theta}_i = \frac{k_\theta}{m_i} \sum_j \sin(\theta_j - \theta_i) + \omega_i + \sqrt{2D_\theta} \xi_\theta, \quad (2)$$

$$\dot{\omega}_i = -\frac{\omega_i}{\tau} + \frac{k_\omega}{m_i} \sum_j (\omega_j - \omega_i) + \xi_b + \sqrt{2D_\omega} \xi_\omega. \quad (3)$$

In equation (1), $\hat{\mathbf{n}}_i$ is a unit vector of orientation θ_i . The mobility μ_i of particle i depends on local polar order P_i near the particle in the linear form of $\mu_i = \Gamma_0(1 + \beta P_i)$; $P_i (\in [0, 1])$ was calculated as $P_i = \langle |\sum_j \frac{\mathbf{r}_j}{|\mathbf{r}_j|} | / m_i \rangle_{t_0}$, where the summation was over m_i particles found in the neighbourhood of particle i (with $|\mathbf{r}_j - \mathbf{r}_i| \leq 5$; including particle i itself), with the angular bracket denoting averaging over time $t_0 = 10$ to smooth out fluctuations. In equations (2) and (3) the summation was also over m_i particles found in the neighbourhood of particle i (with $|\mathbf{r}_j - \mathbf{r}_i| \leq 1$). For the remainder of the equations, k_θ represents the strength of effective polar alignment between velocity directions due to steric and hydrodynamic interactions between cells; k_ω represents the strength of diffusive coupling between angular velocities due to local fluid vorticity; D_r , D_θ and D_ω are translational, rotational and angular velocity diffusivity, respectively; ξ_r , ξ_θ and ξ_ω are Gaussian white noise with zero mean and unit variance; τ arises from the relaxation of local angular velocities; and bias noise $\xi_b = \text{sign}(\omega_i) \exp(-|\omega_i|/\omega_0 \xi)$, where $\text{sign}(\omega_i)$ is the current sign of ω_i , ω_0 is a constant and ξ is a uniform noise in $[0, \eta_{\text{bias}}]$. The signed bias noise term, together with the relaxation term in angular velocity dynamics in equation (3), allows for spontaneous chiral symmetry breaking⁵⁰. Adding finite negative bias b to particles' angular velocity (by substituting ω_i with $(\omega_i + b)$ in equations (2) and (3)—accounting for the swimming bias near a solid substrate⁵¹ shown in Extended Data Fig. 2b)—produced vortex lattice patterns with exclusively clockwise chirality as seen experimentally (Supplementary Information).

In regard to the i -th particle, its position \mathbf{r}_i , orientation θ_i and angular velocity ω_i evolved according to equations (1–3). In equations (2, 3) the coupling range for orientation and angular velocity dynamics was chosen as 1. For each particle, self-propulsion force f_i was sampled from a Gaussian distribution with a mean of f_0 and s.d. of $0.4 f_0$ to account for the heterogeneity of cell motility. We chose the parameters in equation (3) that yielded the temporally averaged angular velocity $\Omega \equiv \langle \omega_i \rangle_{i,t} = -1$. At zero-density limit (that is, without interparticle interactions) the particles move circularly in a clockwise or counterclockwise manner, each following a Gaussian-like local curvature distribution of the same shape (that is, s.d.) and of a mean set by $|\Omega| \equiv |\langle \omega_i \rangle_{i,t}|$; note that the local curvature of the i -th particle's trajectory is proportional to reorientation rate $\Delta\theta_i/\Delta t$ over a finite time based on equation (2). All simulations were initialized with uniform random distributions of particle position, orientation and angular velocity (in the range $[-1, 1]$). For conversion of numbers in particle-based simulations to physical units we set one unit length in the model as $2 \mu\text{m}$ (that is, about one cell length) and one time unit (equivalent to 100 time steps in the simulation) as 1 s. We used particle number $n = 1,600,000$ and size of the system $L_x = L_y = 400$ (with periodic boundary conditions), and thus particle density $\rho_0 = \frac{n}{L_x L_y} = 10$ corresponded to $2.5 \text{ cells } \mu\text{m}^{-2}$ experimentally. To obtain the phase map, mean self-propulsion force f_0 was varied from 1 to 20 and mobility enhancement coefficient β was varied from 0 to 3.0 to be consistent with experimental results. For other simulation parameters the following values were used: $\Gamma_0 = 1$, $k_\theta = 0.2$, $k_\omega = 2$, $D_r = 0.02$, $D_\theta = 0.02$, $D_\omega = 0.02$, $\tau = 10$, $\omega_0 = 0.6$, $\eta_{\text{bias}} = 1.0$. Both Γ_0 and β in the expression of particle speed depend on particle density in accordance with the experimental measurement of cell speed. Because we focus on the phenomenon of single-cell speed increasing with local polar order at a constant cell density in dense suspensions, the model has been designed to describe the emergent dynamics at a relatively high particle density, and the density dependence of model parameters is not considered here.

The collective velocity field $\mathbf{v}(\mathbf{r}, t)$ in particle-based simulations was calculated, based on single-particle velocity ($\mathbf{v}_i(\mathbf{r}, t)$), as $\mathbf{v}(\mathbf{r}, t) = (v_x(\mathbf{r}, t), v_y(\mathbf{r}, t)) = |\sum_i \mathbf{v}_i(\mathbf{r}, t)|/m$, where m is the total number of particles whose position \mathbf{r}_i satisfies $|\mathbf{r}_i - \mathbf{r}| \leq 2$. Similarly, the polar order field was defined as $P(\mathbf{r}, t) = |\sum_i \frac{\mathbf{v}_i(\mathbf{r}, t)}{|\mathbf{v}_i(\mathbf{r}, t)|}|/m$. The vorticity field $\omega(\mathbf{r}, t)$ was calculated based on the computed collective velocity field $\mathbf{v}(\mathbf{r}, t)$ as $\omega(\mathbf{r}, t) = \partial_x v_y(\mathbf{r}, t) - \partial_y v_x(\mathbf{r}, t)$. Particle density field $\rho(\mathbf{r}, t)$

was calculated as $\rho(\mathbf{r}, t) = \frac{N(\mathbf{r})}{\pi d^2}$, where $N(\mathbf{r})$ represented the number of particles whose position \mathbf{r}_j satisfies $|\mathbf{r}_j - \mathbf{r}| \leq d$ ($d = 2$).

To obtain the phase map shown in Fig. 4c we distinguished the mode of emergent collective motion in particle-based simulations by the autocorrelation time of the vorticity field $\omega(\mathbf{r}, t)$. The autocorrelation function of vorticity field is defined as $C_t(\Delta t) = \frac{\langle \omega(\mathbf{r}, t)\omega(\mathbf{r}, t + \Delta t) \rangle_{\mathbf{r}, t}}{\langle \omega(\mathbf{r}, t) \rangle_{\mathbf{r}, t}^2}$, where the angular brackets represent averaging over both the entire simulation domain and time t from 2,000 to 3,000 time units (also keeping $t + \Delta t$ in the same range). The autocorrelation function $C_t(\Delta t)$ was fitted to $C_t(\Delta t)e^{-\Delta t/\tau_0}$, yielding the autocorrelation time τ_0 of the vorticity field. If $\tau_0 \geq 10$ (corresponding to 10 s in experiments), the emergent motion mode was classified as vortex lattice state; otherwise the emergent motion mode was classified as active turbulence state.

We note that, inspired by the nonlinear positive relation between local polar order and collective speed in dense bacterial suspensions reported previously³¹, a power-law-type positive relation between mobility and local polar order $\mu_i \propto P_i^\beta$ ($\beta \geq 0$) could also produce qualitatively similar results in all particle-based simulations.

Numerical simulation of continuum model

In our continuum model, the collective velocity field \mathbf{v} of the quasi-2D bacterial active fluid is governed by the following equation:

$$\partial_t \mathbf{v} + \lambda_0 \mathbf{v} \times \nabla \mathbf{v} = (-\nabla G + \lambda_1 \nabla |\mathbf{v}|^2) - (\alpha + \varphi |\mathbf{v}|^2) \mathbf{v} + \Gamma_1 \nabla^2 \mathbf{v} - \Gamma_2 (\nabla^2)^2 \mathbf{v} + \kappa \omega \mathbf{v}. \quad (4)$$

The core of the equation is the seminal Toner–Tu active fluids model³⁶ and a Swift–Hohenberg-type fourth-order term^{29,52}. Here G is pressure and $(\alpha, \varphi, \lambda_1, \kappa, \Gamma_1, \Gamma_2, \lambda_0)$ are model parameters with the latter three related to the effective viscosity of the active fluid, η_{eff} (which is inversely proportional to single-cell mobility μ)³⁸: $\Gamma_1 = -\gamma_1 \Gamma_0 / \eta_{\text{eff}}$, $\Gamma_2 = \gamma_2 \Gamma_0 / \eta_{\text{eff}}$ and $\lambda_0 = (1 - S\eta_0 / \eta_{\text{eff}})$, with $\gamma_1, \gamma_2, \Gamma_0, \eta_0$ and ϵ being constants; in the last expression S is the activity parameter ($S < 0$ for pusher-type swimmers such as *S. marcescens*)¹⁸ and η_0 is effective zero-shear viscosity. The system is treated as an incompressible fluid (that is, $\nabla \times \mathbf{v} = 0$). To account for the behaviour of self-enhanced mobility, η_{eff} is taken to depend on local polar order P as $\eta_{\text{eff}} = \eta_0 / (1 + \beta P)$ and it can be expressed in terms of $|\mathbf{v}|$ (noting the collective speed $|\dot{\mathbf{v}}| \propto \mu P = P / \eta_{\text{eff}}$). In addition, the vorticity-dependent term $\kappa \omega \mathbf{v}$ (ω is vorticity of the velocity field) allows chirality selection depending on the sign of parameter κ , which accounts for the chirality bias observed experimentally; note that the system shows spontaneous chiral symmetry breaking at $\kappa = 0$ (that is, the emergent vortex lattice pattern has an equal probability of being clockwise or anticlockwise).

The velocity field $\mathbf{v}(\mathbf{r}, t) = (v_x(\mathbf{r}, t), v_y(\mathbf{r}, t))$ in equation (4) was solved numerically using the pseudo-spectral method⁵³. Vorticity field ω was calculated based on computed velocity field \mathbf{v} as $\omega = \partial_x v_y - \partial_y v_x$. The incompressibility condition $\nabla \times \mathbf{v} = 0$ was enforced by correcting the gradient of hydrodynamic pressure at every time step using the Lagrange multiplier⁵⁴. All equations were solved or integrated in Fourier space except for the computation of nonlinear terms⁵⁴. Velocity field was inversely transformed back to real space for visualization. Velocity field $\dot{\mathbf{v}}$ evolved in 2D cubic grids with a size of $n_x \times n_y = 256 \times 256$ lattice points. System size $L_x = L_y = 44\pi$ (with periodic boundary conditions) and time step $dt = 0.00001$ were used in the simulations.

Mobility enhancement coefficient β and activity $|S|$ were varied from 0 to 3.0 (to be consistent with experimental results). All simulations were initialized with uniform random distributions of velocity direction in $[0, 2\pi]$ and velocity magnitude in $[0, 1]$. For other simulation parameters the following values were used: $\alpha = 0.2$, $\varphi = 0.01$, $\gamma_1 = 2$, $\gamma_2 = 1$, $\Gamma_0 = 1$, $\eta_0 = 1$, $\epsilon = 1$ and $\kappa = -0.1$. Simulations of the continuum model were written in C++ and performed on NVIDIA GeForce RTX 2080Ti through the application programming interface (API) of the Compute Unified Device Architecture toolkit and platform.

Finally, similar to particle-based simulations, we note that a power-law-type relation between effective viscosity and local polar order, $\eta_{\text{eff}} = \eta_0 P^{-\beta} \propto |\mathbf{v}|^{-\beta/(1+\beta)}$ ($\beta \geq 0$), could also produce qualitatively similar results in all continuum simulations.

Data availability

The data supporting the findings of this study are included within the paper and its Supplementary Information.

Code availability

The custom codes used in this study are available from the corresponding author on request.

48. Mukherjee, A., Walker, J., Weyant, K. B. & Schroeder, C. M. Characterization of flavin-based fluorescent proteins: an emerging class of fluorescent reporters. *PLoS ONE* **8**, e64753 (2013).
49. Zuo, W. & Wu, Y. Dynamic motility selection drives population segregation in a bacterial swarm. *Proc. Natl Acad. Sci. USA* **117**, 4693–4700 (2020).
50. Chen, C., Liu, S., Shi, X. Q., Chate, H. & Wu, Y. Weak synchronization and large-scale collective oscillation in dense bacterial suspensions. *Nature* **542**, 210–214 (2017).
51. Lauga, E., DiLuzio, W. R., Whitesides, G. M. & Stone, H. A. Swimming in circles: motion of bacteria near solid boundaries. *Biophys. J.* **90**, 400–412 (2006).
52. Swift, J. & Hohenberg, P. C. Hydrodynamic fluctuations at the convective instability. *Phys. Rev. A* **15**, 319–328 (1977).
53. Banerjee, D., Souslov, A., Abanov, A. G. & Vitelli, V. Odd viscosity in chiral active fluids. *Nat. Commun.* **8**, 1573 (2017).
54. Danaila, I., Joly, P., Kaber, S. M., Postel, M. (eds) *An Introduction to Scientific Computing: Twelve Computational Projects Solved with MATLAB* (Springer, 2007).

Acknowledgements We thank A. Mukherjee and C. M. Schroeder (University of Illinois at Urbana-Champaign) and H. Berg (Harvard University) for generous gifts of bacterial strains. We thank Y. Wang (The Chinese University of Hong Kong) for help with computing resources and R. Zhang (HKUST) for helpful discussions on numerical simulations. This work was supported by the Ministry of Science and Technology of China (no. 2020YFA0910700), the Research Grants Council of Hong Kong SAR (RGC ref. nos. 14307821, 14307822, RFS2021-4S04 and CUHK Direct Grants) and the National Natural Science Foundation of China (NSFC no. 31971182). Y.W. acknowledges support from New Cornerstone Science Foundation through the Xplorer Prize.

Author contributions H.X. discovered the phenomena, designed the study, performed experiments, developed the model, performed simulations and analysed and interpreted the data. Y.W. conceived the project, designed the study and analysed and interpreted the data. Y.W. and H.X. wrote the paper.

Competing interests The authors declare no competing interests.

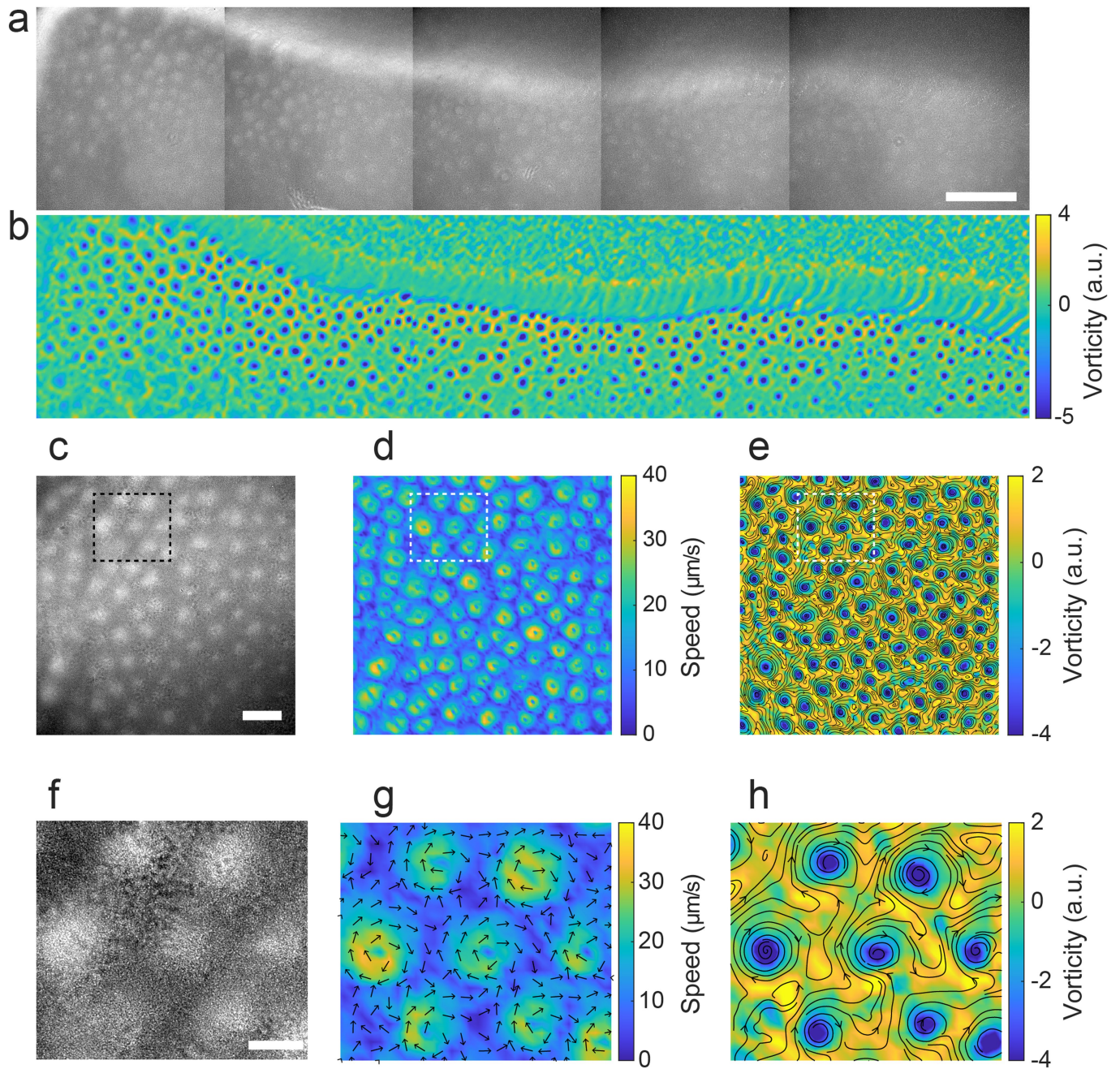
Additional information

Supplementary information The online version contains supplementary material available at <https://doi.org/10.1038/s41586-024-07114-8>.

Correspondence and requests for materials should be addressed to Yilin Wu.

Peer review information *Nature* thanks the anonymous reviewers for their contribution to the peer review of this work. Peer reviewer reports are available.

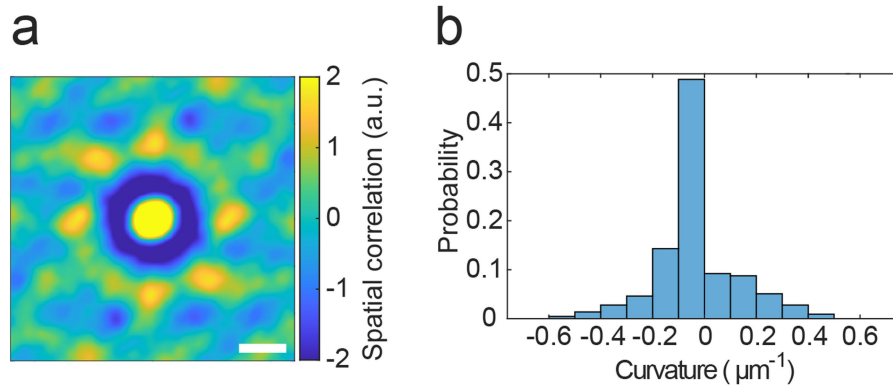
Reprints and permissions information is available at <http://www.nature.com/reprints>.



Extended Data Fig. 1 | Vortex lattice pattern at different length scales.

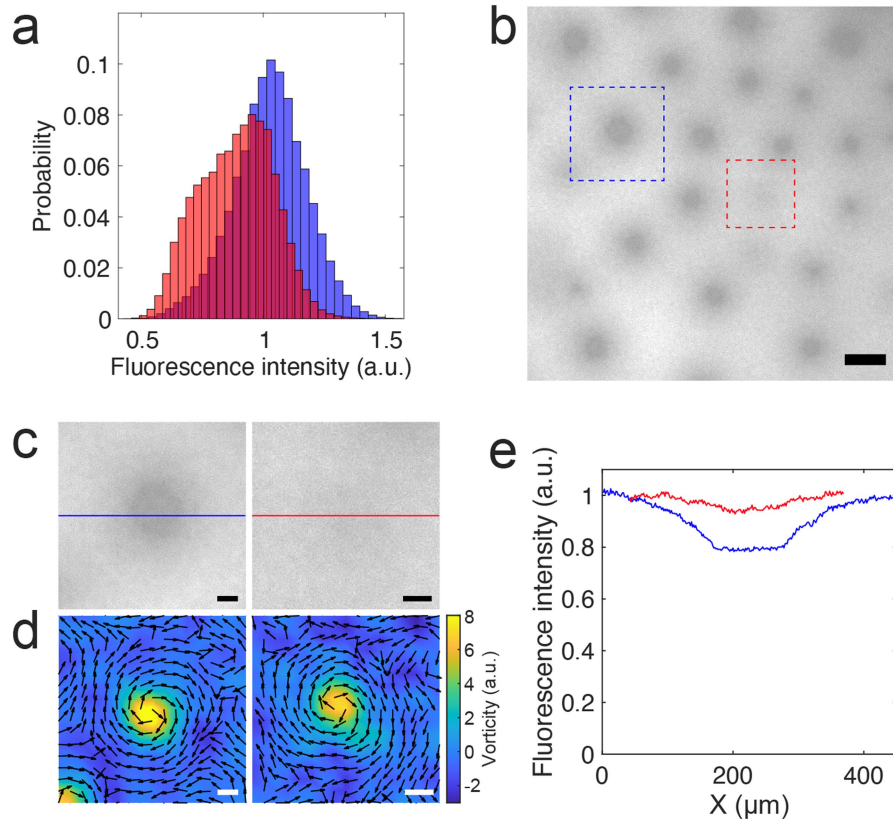
(a) Vortex lattice pattern at centimeter scale. Upper: phase-contrast image; lower: vorticity field associated with the phase-contrast image, computed based on the collective velocity field. The length and width of the panel is -1.4 cm and 3.3 mm, respectively. The upper panel is a composite image obtained by stitching a sequence of 5 images taken at connected smaller windows; for each window, a short video lasting -10 s was taken to compute the collective velocity field via PIV (Methods). The vortices appeared everywhere in the image except at the upper region; this region is close to the edge of the

suspension film, where the fluid film has a greater thickness. The vortices at the rightmost region in the phase-contrast image (upper panel) are not apparent because the cell densities inside and outside the vortices are similar, but they can be visualized in the vorticity field (lower panel). Scale bar, 1 mm. (b-d) Phase-contrast image (panel c), collective speed distribution (panel d), and vorticity distribution (panel e) of the vortex lattice pattern shown in main text Fig. 1a-c. Panels b-d share the same scale bar (500 μm). (e-g) Enlarged view of the area enclosed by the box in panels b-d. The arrows in panel f represent the velocity direction of the local collective velocity. Scale bar, 200 μm.



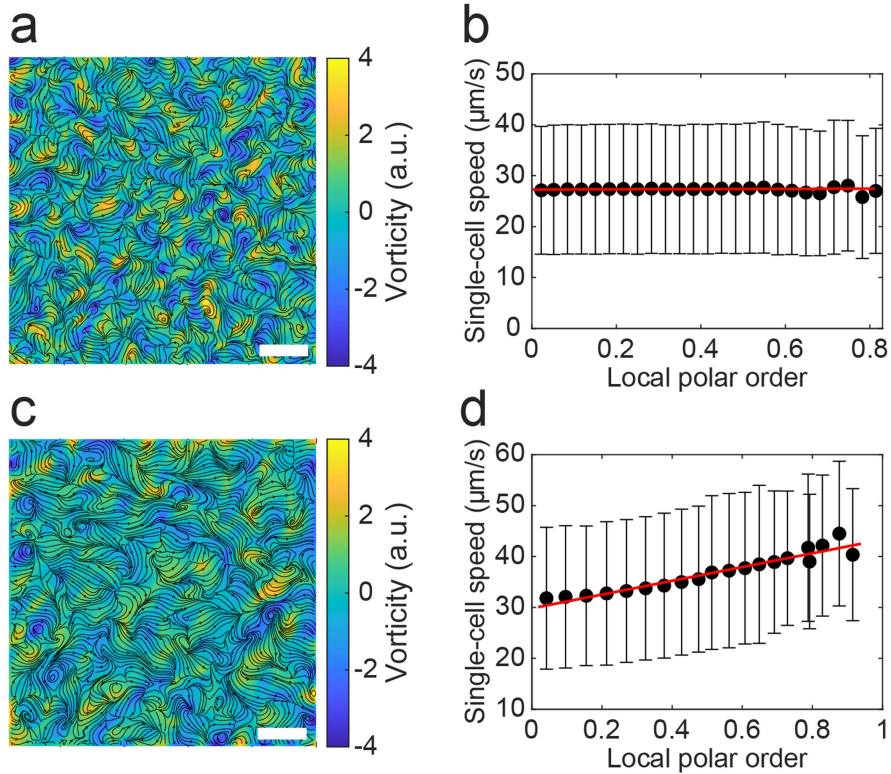
Extended Data Fig. 2 | Spatial correlation of the vorticity field and motion bias of isolated *S. marcescens* cells. (a) Spatial correlation of the vorticity field in a quasi-2D dense bacterial active fluid. This panel is associated with main text Fig. 1a–c (Methods). Colorbar provided to the right is in arbitrary unit. Scale bar, 200 μm . (b) Motion bias of isolated *S. marcescens* cells swimming near a solid substrate. This panel shows the probability distribution of the signed curvature of single-cell trajectories near a solid substrate, with the mean curvature being $-0.023 \mu\text{m}^{-1}$. The signed curvature of cell trajectories was computed based on

1-s segments of cell trajectories (positive: CCW; negative: CW). To obtain the distribution, cells were extracted from dense *S. marcescens* suspensions that displayed the large-scale ordered vortex lattice, diluted to an appropriate density, and deposited on freshly made 0.6% LB agar surface to form a quasi-2D dilute bacterial suspension drop. *S. marcescens* cells in the prepared suspension drop were tracked in fluorescence microscopy, while the environmental temperature was maintained at 30 $^{\circ}\text{C}$ with a custom-built temperature-control system (Methods).



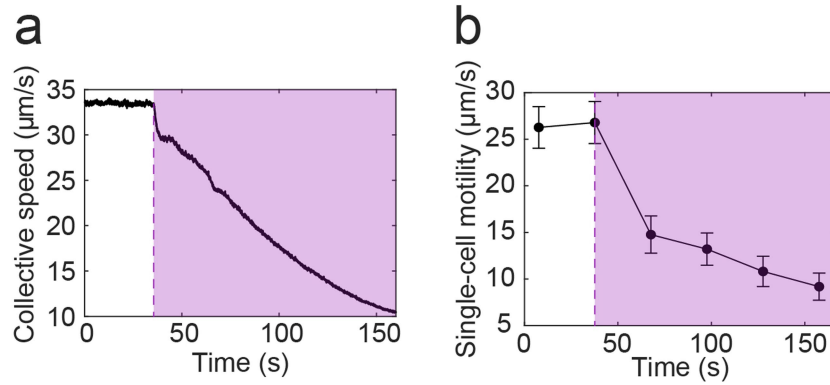
Extended Data Fig. 3 | Characterization of cell density distribution in the vortex lattice pattern. (a) Probability distributions of fluorescence intensity inside (red) and outside (blue) the vortices in a representative vortex lattice pattern. Fluorescence intensity is a measure of cell density because cells were labelled by GFP. The averaged density difference between inside and outside vortices of the vortex lattice pattern obtained from the fluorescence intensity distributions is -15%. (b) Spatial distribution of the fluorescence intensity in the vortex lattice pattern analyzed in panel a. The cell density inside vortices is slightly lower than or comparable to the regions outside the vortices. Scale bar, 200 μm . (c) Enlarged view of the areas enclosed by the boxes in panel b. Each box contains a vortex. Left (blue box in panel b): the cell density inside the

vortex is slightly lower than outside; right (red box in panel b): the cell density inside the vortex is similar to outside. (d) Vorticity fields corresponding to the regions shown in panel c. Color bar represents the magnitude of vorticity while the arrows represent the direction of local collective velocity vectors. The vorticity fields for the two vortices are similar, suggesting that cell density difference is not necessary for vortex formation. Scale bars in panel c and d, 50 μm . (e) Fluorescence intensity plotted along the straight lines across the two vortices in panel c. The red and blue plots in panel e were plotted along the lines with the respective color in panel c. Data shown in the plots were normalized by the mean fluorescence intensity in regions outside the vortices.



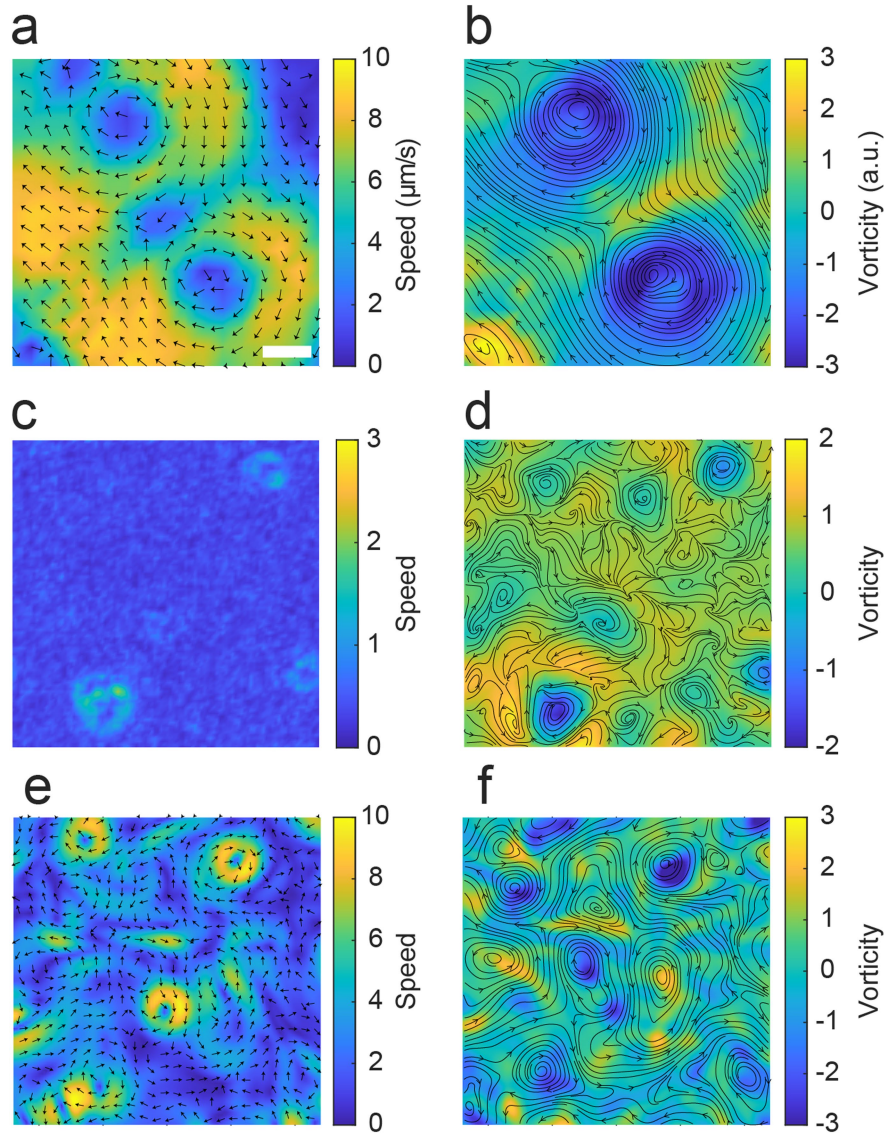
Extended Data Fig. 4 | Behavior of quasi-2D bacterial active fluids below the critical cell density for developing ordered vortex lattice. (a,c) Spatial distribution of instantaneous vorticity computed based on collective velocity field of bacterial active fluids (panel a: 2.0×10^{10} cells/mL; panel c, 3.7×10^{10} cells/mL). The vorticity fields are plotted in the same manner as in main text Fig. 1c. Both panels show disordered spatial distribution of vortices. Panels a and c share the same scale bar (500 μm). (b,d) Apparent single-cell speed

plotted against local polar order (as a proxy of local collective active stress) in bacterial active fluids (panel b: 2.0×10^{10} cells/mL; panel d, 3.7×10^{10} cells/mL). In panel b, single-cell speed is almost independent of local polar order (i.e., the mobility enhancement coefficient $\beta \approx 0$). In panel d, single-cell speed is weakly correlated with local polar order ($\beta \approx 0.48$). Error bars in panel b and d indicate standard deviation ($N > 50$ single-cell trajectories for each data point).



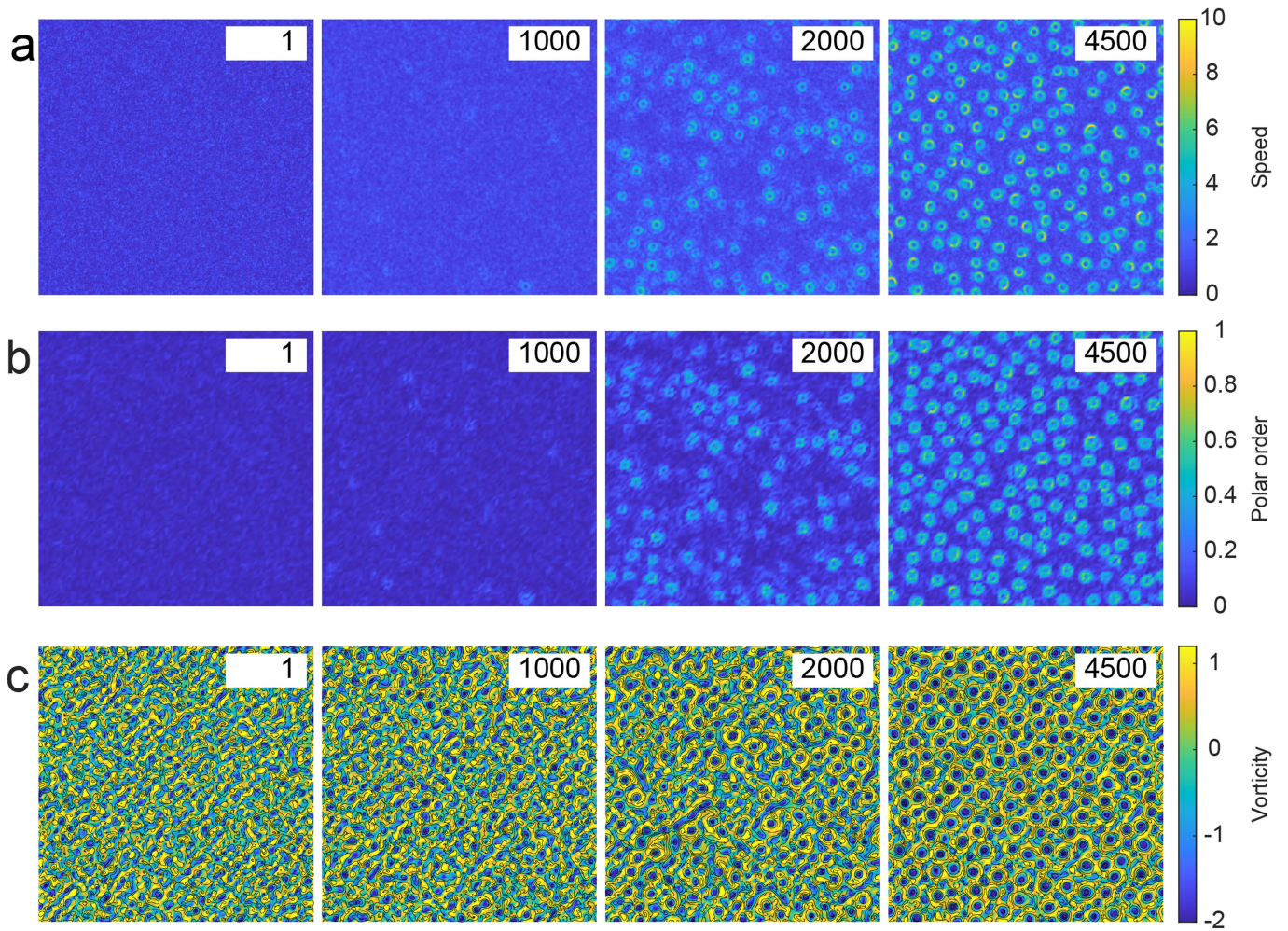
Extended Data Fig. 5 | Suppression of bacterial motility by violet light illumination. (a) Collective speed averaged over the entire field of view was plotted as a function of time. The vortex lattice was illuminated by violet light at $T = 35.5$ s (violet dashed line) and the motility of all cells in the entire field of view was suppressed by violet light illumination. This figure is associated with Video S3. (b) Tuning single-cell motility of *S. marcescens* via violet-light illumination. Single-cell motility refers to the intrinsic speed cells in an isolated environment; it is different from the apparent single-cell speed measured in dense suspensions where cell's motion is affected by the mechanical environment. To measure single-cell motility, cells were extracted from dense *S. marcescens* suspensions that displayed the large-scale ordered vortex lattice, diluted to an appropriate density, and deposited on freshly made 0.6% LB agar surface to form a quasi-2D dilute bacterial suspension drop. *S. marcescens* cells in the prepared suspension drop were tracked in fluorescence microscopy

through a 20x objective lens, and starting from $T = 35.5$ s the cells were continuously illuminated by 406 nm violet light (Methods). The environmental temperature was maintained at 30 °C with a custom-built temperature-control system (Methods). The speed of an isolated cell (i.e., the motility of the cell) at a specific time T was computed based on its trajectory tracked from $(T-0.5)$ s to $(T+0.5)$ s; the speeds of isolated cells computed from $(T-12.5)$ s to $(T+12.5)$ s were then averaged and taken to be the mean of single-cell motility at time T . Before violet-light illumination, the temporal variation of the speed of isolated cells is -17%, suggesting that cells prepared from the same overnight culture should have a similar self-propulsion force. Data presented in this figure show that the average collective speed measured in the dense suspension (panel a) is proportional to single-cell motility (panel c) measured in isolated environment during violet light illumination. Therefore, the average collective speed is an appropriate proxy of single-cell motility.



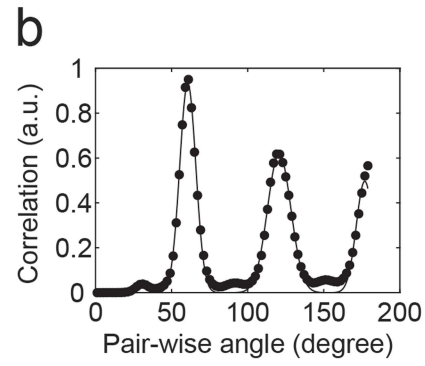
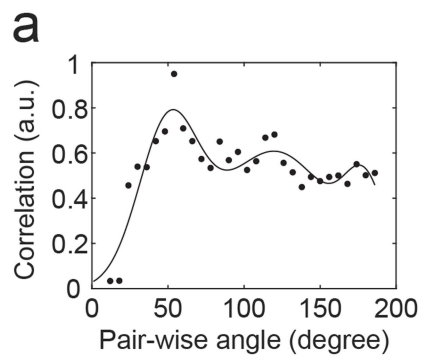
Extended Data Fig. 6 | Sporadic vortices in quasi-2D dense *E. coli* suspensions and in numerical simulations. (a,b) Time-averaged collective velocity field (panel a) and vorticity field (panel b) experimentally measured in a dense *E. coli* suspension (Methods) showing sporadic and disordered vortices. Isolated *E. coli* cells have a mean speed of $-10 \mu\text{m/s}$ (versus $-25 \mu\text{m/s}$ for isolated cells of *S. marcescens*). Data presented in the two panels were averaged over a duration of 10 s. In panel a, arrows and colormap represent collective velocity directions and magnitude, respectively, with the colorbar provided to the right, in unit of $\mu\text{m/s}$. Panels a,b share the same scale bar, $500 \mu\text{m}$. Also see Video S4. (c,d) Time-averaged particle speed spatial distribution (panel c) and vorticity

field (panel d) showing sporadic and disordered vortices in particle-based simulation with a low particle activity (simulation parameters: $f_0 = 7$ and $\beta = 1.2$). Data were averaged over a duration of 10 time units. Colormap in panel c represents particle speed, with the colorbar provided to the right. (e,f) Time-averaged collective velocity field (panel e) and vorticity field (panel f) showing sporadic and disordered vortices in continuum modeling with a low activity (simulation parameters: $|S| = 2.6$ and $\beta = 2.0$). Data were averaged over a duration of 10 time units and plotted in the same manner as panels a,b. The simulation parameter sets in panels c,d and e,f were chosen from the boundary between the active turbulence state and the vortex lattice state in Fig. 4c and Fig. 4f, respectively.



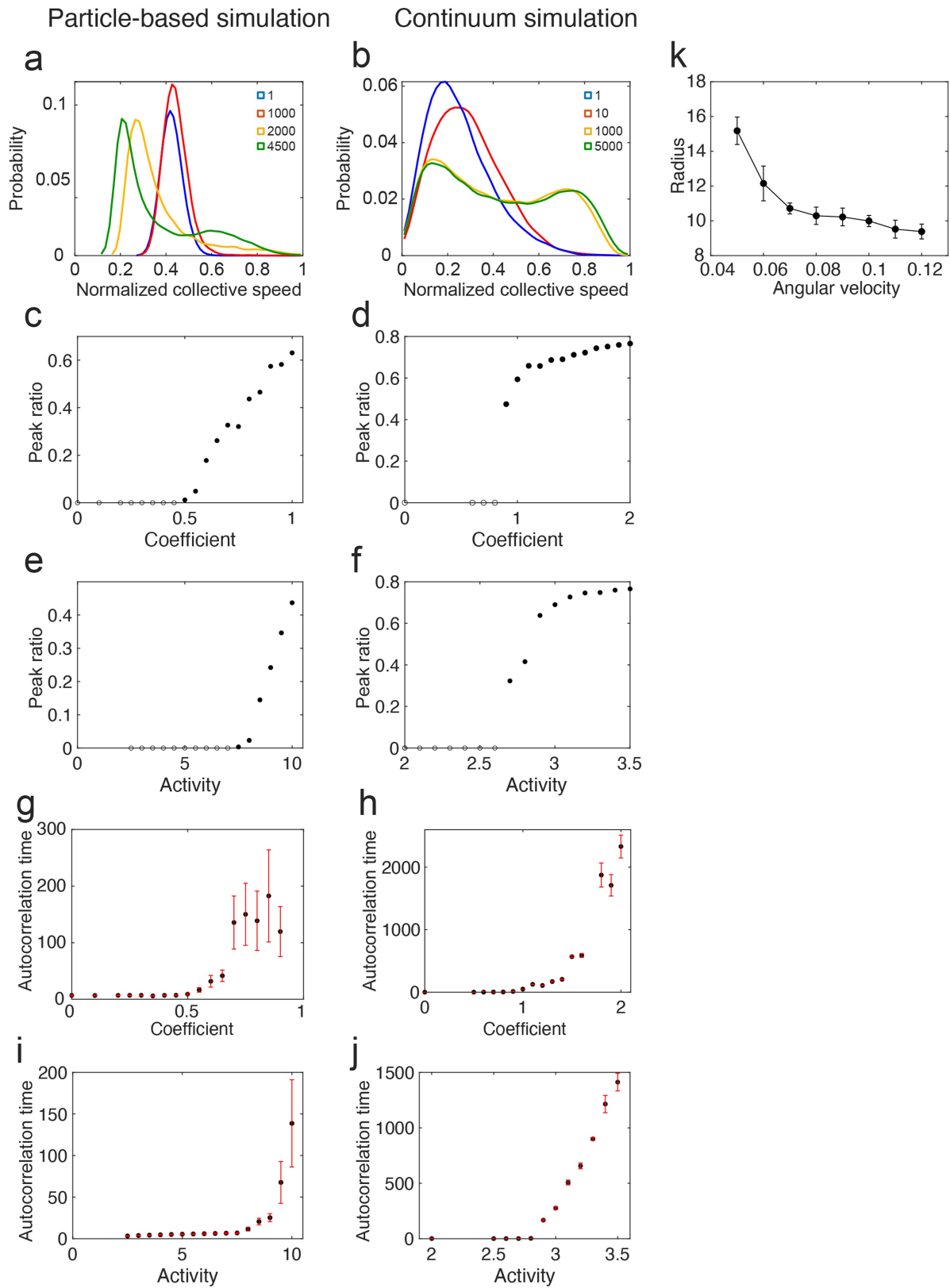
Extended Data Fig. 7 | Emergence of vortex lattice pattern in the particle-based simulation. Time sequence of spatial distributions of instantaneous collective speed (panel a), local polar order (panel b), and vorticity (panel c) during the emergence of ordered vortex lattice in the particle-based simulation. The magnitude of particle speed, local polar order and vorticity is indicated by

the colorbars provided to the right of each panel. The vorticity field shown in panel c was plotted in the same manner as in main text Fig. 1c. The time stamp in each sub-panel indicates the elapsed time units in the simulation. Simulation parameters: particle activity $f_0 = 10$ and mobility enhancement coefficient $\beta = 1.2$. This figure is associated with main text Fig. 4d,e.



Extended Data Fig. 8 | Triplet-distribution function in particle-based (panel a) and continuum (panel b) simulations. Solid lines were obtained by fitting the data into a sum of three Gaussian functions (Methods). Simulation parameters were identical to those used in main text Fig. 4d,e and Fig. 4g,h,

respectively: particle activity $f_0 = 10$ and mobility enhancement coefficient $\beta = 1.2$ in panel a; activity $|S| = 3.5$ and mobility enhancement coefficient $\beta = 2.0$ in panel b.

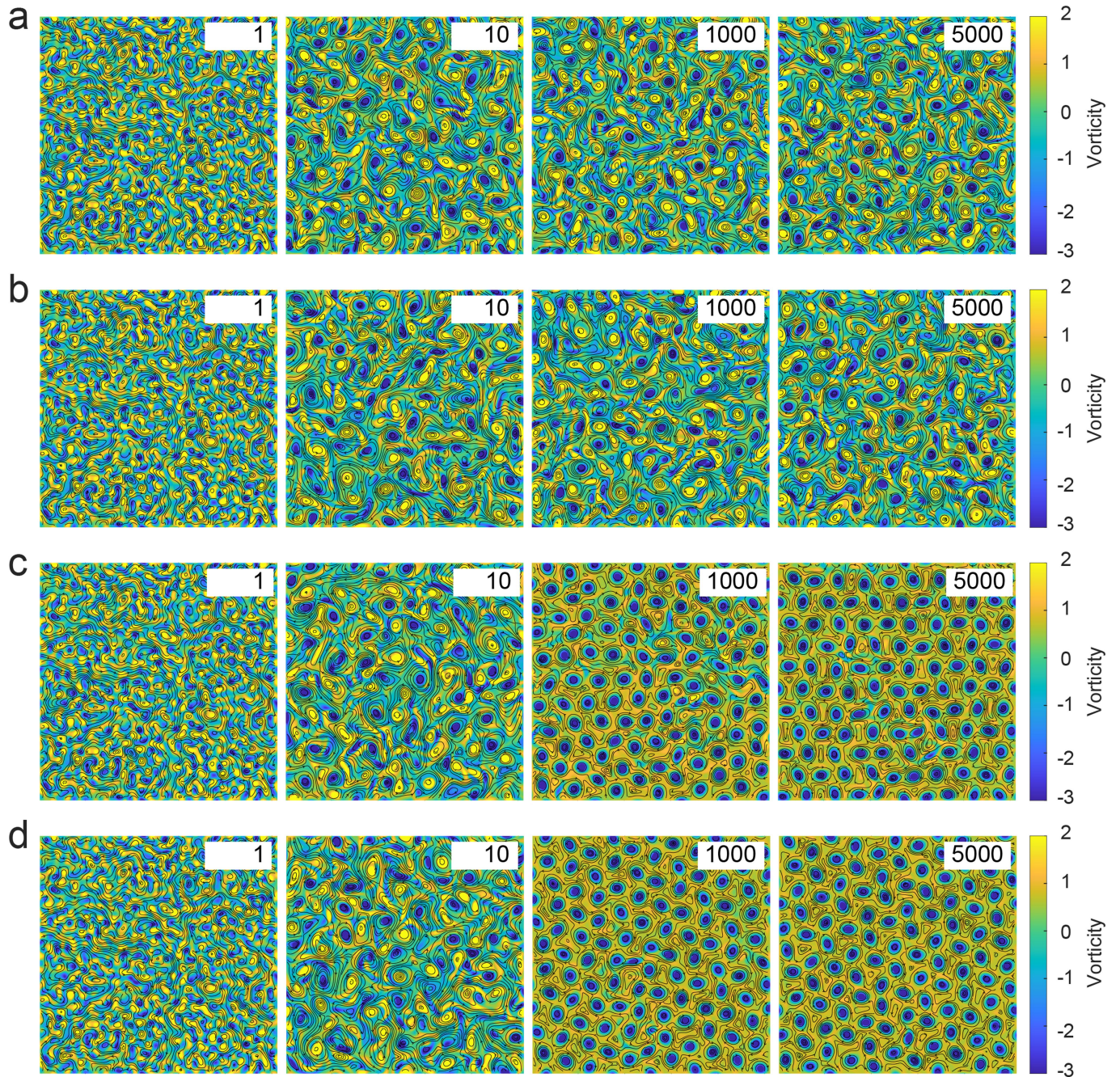


Extended Data Fig. 9 | See next page for caption.

Extended Data Fig. 9 | Characterization of signatures for the transition to stable vortex lattice state in particle-based and continuum modeling.

Panels a, c, e, g, i: results from particle-based simulations; panels b, d, f, h, j: results from continuum simulations. **(a, b)** Probability distributions of normalized particle speed (panel a) and of collective speed (panel b) during the emergence of vortex lattice pattern (in comparison with Fig. 3c). The colors represent time units elapsed in the simulations. Simulation parameters: $f_0 = 10$ and $\beta = 1.2$ in panel a; $|S| = 3.5$ and $\beta = 2.0$ in panel b. **(c, d)** Peak ratio in collective speed distribution (Methods) plotted against β (in comparison with Fig. 3e). **(e, f)** Peak ratio in collective speed distribution plotted against the f_0 (panel e) and against $|S|$ (panel f) (in comparison with Fig. 3f). **(g, h)** Steady-state autocorrelation time of collective velocity (as a measure of vortex lifetime; Methods) plotted against β (in comparison with Fig. 3d). **(i, j)** Steady-state

autocorrelation time of collective velocity plotted against f_0 (panel i) and against $|S|$ (panel j). In panel c-f, the solid circles represent data from bimodal speed distributions, while the empty circles correspond to zero peak ratio and represent data from unimodal speed distributions (i.e., the higher-speed peak has a height of zero). Simulation parameters: $f_0 = 10$ and β from 0 to 1.0 for panels c, g; f_0 from 2 to 10 and $\beta = 0.8$ for panels e, i; $|S| = 3.5$ and β from 0 to 2 for panels d, h; $|S|$ from 2 to 3.5 and $\beta = 2.0$ for panels f, j. **(k)** Mean radius of vortices is negatively correlated with the mean angular velocity of particles ($\Omega = \langle \omega_i \rangle_t$) in a simplified particle-based model, where the time evolution of particle angular velocity ω_i (Eq. [3] in Methods) is replaced by drawing its value from a distribution derived from Extended Data Fig. 2b. Error bars represent the standard deviation, $N = 20$. Simulation parameters: $f_0 = 10$ and $\beta = 1.2$.



Extended Data Fig. 10 | Emergence of collective motion patterns in the continuum model. This figure shows the time sequences of vorticity field in numerical simulations of the continuum model with different mobility enhancement coefficient ($\beta=0, 0.5, 1.0$ and 2.0 for panels a, b, c and d,

respectively; activity $|S|=3.5$ for all panels). The time stamp in each sub-panel indicates the elapsed time units in the simulation. The vorticity fields are plotted in the same manner as in main text Fig. 1c.